SuperDARN observations during geomagnetic storms, geomagnetically active times and enhanced solar wind driving

M.-T. Walach[1], **A. Grocott**[1]

[1]Lancaster University, Bailrigg, Lancaster, LA1 4YW, United Kingdom

Key Points:

- During geomagnetic storms and enhanced solar wind driving ionospheric convection expands to latitudes as low as 40° magnetic latitude.
- Initial and recovery phases of geomagnetic storms show similar convection as enhanced solar wind driving when no geomagnetic storm occurs.
- Main phase shows most scatter, fastest flows (CPCP ~80 kV instead of ~40 kV during initial and recovery) due to higher solar wind driving.

Corresponding author: M.-T. Walach, `m.walach@lancaster.ac.uk`

Abstract

The Super Dual Auroral Radar Network (SuperDARN) was built to study ionospheric convection at Earth and has in recent years been expanded to lower latitudes to observe ionospheric flows over a larger latitude range. This enables us to study extreme space weather events, such as geomagnetic storms, which are a global phenomenon, on a large scale (from the pole to magnetic latitudes of 40°). We study the backscatter observations from the SuperDARN radars during all geomagnetic storm phases from the most recent solar cycle and compare them to other active times to understand radar backscatter and ionospheric convection characteristics during extreme conditions and to discern differences specific to geomagnetic storms and other geomagnetically active times. We show that there are clear differences in the number of measurements the radars make, the maximum flow speeds observed and the locations where they are observed during the initial, main and recovery phase. We show that these differences are linked to different levels of solar wind driving. We also show that when studying ionospheric convection during geomagnetically active times, it is crucial to consider data at mid-latitudes, as we find that during 19% of storm-time the equatorward boundary of the convection is located below 50° of magnetic latitude.

1 Introduction

Geomagnetic storms are one of the more extreme examples of geomagnetic responses to solar wind driving. Typically, they are driven by interplanetary coronal mass ejections (ICMEs) or interplanetary co-rotating interaction regions (CIRs) in the solar wind and result in strong enhancements in the radiation belt region around the Earth (e.g. Gonzalez et al., 1994; Gonzalez, Tsurutani, & Clúa de Gonzalez, 1999; Kilpua, Balogh, von Steiger, & Liu, 2017; Turner et al., 2019, and references therein). Sheath regions, which precede ICMEs in the solar wind, are often associated with fast solar wind, shock fronts and followed by magnetic clouds, which manifest themselves as prolonged intervals of strong and steady interplanetary magnetic field (IMF) (e.g. Kilpua et al., 2017, and references therein). Southward IMF in particular is known to be an important driver of activity in the magnetospheric-ionospheric system, which manifests itself as enhanced plasma transport through the magnetosphere due to an increase in dayside reconnection rates (e.g. Cowley & Lockwood, 1992; Milan, 2015; Milan, Gosling, & Hubert, 2012; Walach, Milan, Yeoman, Hubert, & Hairston, 2017, and references therein). This is particularly relevant for geomagnetic storms, as it has been shown that the recovery phase of a storm, when the geomagnetic activity decreases, is coupled to a decrease in southward IMF and thus solar wind driving (Gonzalez et al., 1999). After a period of southward IMF (or solar wind driving) and open flux accumulation known as the growth phase, explosive unloading events, known as substorms follow (e.g Baker, Pulkkinen, Angelopoulos, Baumjohann, & McPherron, 1996; McPherron, 1970). Following substorm onset, the polar cap decreases in size as nightside reconnection dominates over dayside reconnection (Milan, Hutchinson, Boakes, & Hubert, 2009; Milan, Provan, & Hubert, 2007). As this happens, particles are injected on the nightside into the inner magnetosphere. Whilst substorms may be critical in energising the ring current (Kamide et al., 1998), it has been shown that the Dst ring current index, which is similar to the Sym-H index (Wanliss & Showalter, 2006), can be simulated well using solar wind data alone (O'Brien & McPherron, 2000). This is no coincidence, as substorms are also driven by the solar wind.

Hutchinson, Wright, and Milan (2011) identified geomagnetic storms over a solar cycle and split them into categories of strength as well as storm phases: The initial phase, main phase and recovery phase. The initial phase is accompanied by increases in solar wind pressure, often associated with a CME or CIR and causes a compression of the magnetosphere on the dayside, resulting in positive increases to Sym-H. The main phase then follows when solar wind driving (i.e. dayside reconnection) is high depositing a large amount of energy, of the order of a few 10^{31} keV, into the magnetosphere (Kozyra et al., 1998). The ring current is then enhanced, which we see in a sudden depression in Sym-H. The main phase is followed by a recovery phase, which occurs due to a decrease in solar wind driving and is marked by a return to less enhanced values of Sym-H. Contrary to a previous result by Yokoyama and Kamide (1997), Hutchinson, Wright, and Milan (2011) showed that the average length of the main phase of a geomagnetic storm is anti-correlated with the intensity of a geomagnetic storm (given by the Sym-H minimum), whereas the duration of the recovery phase is correlated with the magnitude of the geomagnetic storm.

Hutchinson, Grocott, Wright, Milan, and Boakes (2011) used the same geomagnetic storm list to study ionospheric convection during storms, although they did not attempt to compare their observations to those made during intervals with similar solar wind driving, or geomagnetic activity in general. They used the Super Dual Auroral Radar Network (SuperDARN), which is an international network of ground-based high-frequency radars, built for the purpose of studying ionospheric convection (Chisham et al., 2007;

Greenwald et al., 1995). They also looked at auroral data from the Imager for Magnetopause-to-Aurora Global Exploration (IMAGE) satellite (Mende et al., 2000) in conjunction with the radar data. They showed that the latitudinal extent of the return flow region maps well to the auroral region on the nightside during geomagnetic storms, although their analysis only extended to 50° magnetic latitude due to the years of study being limited to 1997-2008. For the most recent years of SuperDARN data, this has been expanded to 40° as a result of building new mid-latitude radars, which we utilise here.

To look at how the ionosphere responds during geomagnetic storms of the most recent solar cycle, we use SuperDARN data from the years 2010-2016 to study high-latitude ionospheric convection in a holistic way. We address a number of questions, for example: Do we make similar SuperDARN observations during similar solar wind driving during non-storm time as during storm time? Do SuperDARN observations change throughout the different phases of a storm? Where do we see the fastest flows with SuperDARN and is it linked to the extent of latitudinal coverage from the radars? Does the latitudinal range of the convection, given for example by the return flow region, stay constant throughout a storm?

In this paper, we will compare ionospheric convection parameters and features during geomagnetic storms and geomagnetically active times when the Sym-H index is enhanced, as well as times when solar wind driving is high, but geomagnetic activity is low. Periods of solar wind driving typically lead to substorms, but in this case we will only select periods of driving that are not sufficiently driven for geomagnetic storms to occur. We will discuss the selection criteria in the next section.

2 Data selection

In this section we introduce the primary datasets used for this study: the geomagnetic storm data, and the SuperDARN radar data.

2.1 Geomagnetic storm data

Our storm identification procedure is similar to that of Hutchinson, Wright, and Milan (2011), which provides us with a way of comparing our event distribution.

Each storm is found and divided into storm phases, using an automated algorithm, as illustrated in Figure 1. The minimum in Sym-H of each storm is found, which marks the beginning of the recovery phase and the end of the main phase. The end of the recovery phase is marked by the point where Sym-H reaches the quiet level (-15 nT) thereafter. The beginning of the main phase is marked by the last point where Sym-H crosses the quiet level prior to the minimum. From there, we then find the maximum in Sym-H above the quiet level phase, prior to the main phase with a maximum time separation of 18 hours between the maximum and the start of the main phase. To find the beginning of the initial phase, we simply find where Sym-H reaches a quiet level, before the maximum of the initial phase occurs. This ensures that we do not miss any storm sudden commencements or sudden impulses. The only difference between our algorithm and the one from Hutchinson, Wright, and Milan (2011) is the definition of the start of the main phase. We use the crossing of the quiet level, whereas they use the maximum in Sym-H. The main reason for choosing this, was that when we inspected the Sym-H traces of the storms visually, the maximum in Sym-H during the initial phase was not always very clearly defined, whereas the crossing of the quiet level is always very clear.

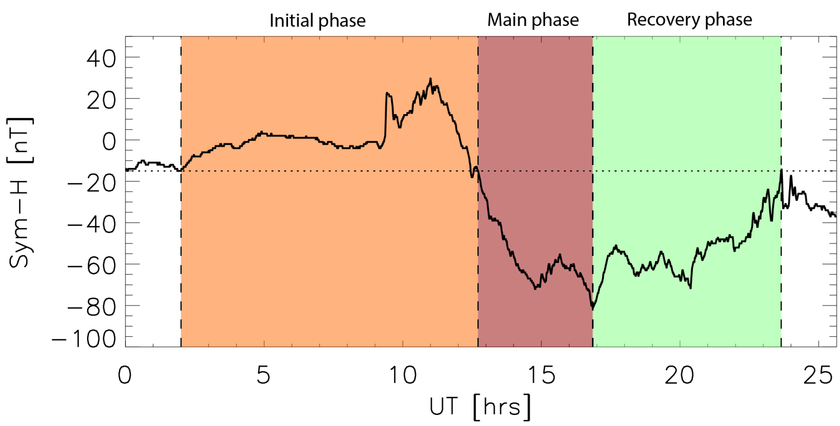

Figure 1. Figure showing typical Sym-H trace of a geomagnetic storm. The colours show our phase identification with the initial phase in orange, the main phase in red and the recovery phase in green.

We have divided our storms into the same categories as Hutchinson, Wright, and Milan (2011) for comparative purposes, but look at the more recent solar cycle (2010-2016) instead of 1997-2008.

In our study, we have 43 weak storms (-150 nT $<$ Sym-H < -80 nT), 5 moderate storms (-300 nT $<$ Sym-H < -150 nT) and no intense storms (Sym-H < -300 nT), whereas Hutchinson, Wright, and Milan (2011) found 8 intense storms during the years of 1997-2008. It is worth noting however that this is not a problem: As we will show later, the convection pattern reaches the observable limit for our storm list, reaching 40° magnetic latitude for moderate storms, 10° lower than Hutchinson, Wright, and Milan (2011) could observe, so it is highly unlikely that we or they could accurately inspect the intense category. Overall, their study also contains more storms in general: 143 storms, as opposed to our 48 storms. This means Hutchinson, Wright, and Milan (2011) observed on average 12 geomagnetic storms per year, whereas we found 8 per year on average. This is likely due to the fact that the most recent solar cycle has been weaker than the previous one with less solar wind driving of the magnetosphere (Selvakumaran et al., 2016). It was found by Gillies, McWilliams, St. Maurice, and Milan (2011) that geomagnetic storms are a continuum of intensities, rather than separate classes. Furthermore, they found that the Sym-H index responds predictably to the strength of the southward IMF, regardless of storm driver. As such, we will not discuss storm drivers or classes any further, but rather focus on comparing storm characteristics during the different storm phases to geomagnetically active times in general and other times of solar wind driving.

To select times when solar wind driving is high and similar to the solar wind conditions during storms, we set a lower threshold for the solar wind speed ($V_{SW} \geq 350$km/s), the total magnetic field component of the IMF ($B_{TOT} > 8$nT), and the absolute of the clock angle ($|\theta| > 100°$). We also specify that for these conditions, no geomagnetic storm must occur (Sym-H> -80nT). These selection criteria were chosen such that the driving conditions are similar to a geomagnetic storm, as we will later see in Fig. 3. Additionally, to investigate the significance of storms and storm phase on the ionospheric convection, we also compare to times of high geomagnetic activity (SYM-H<-80nT), but in this case not binned by storm phase.

2.2 SuperDARN radar data

The Super Dual Auroral Radar Network (SuperDARN) is an international network of ground-based high-frequency radars located in the auroral regions of the northern and southern hemispheres (Chisham et al., 2007; Greenwald et al., 1995). Transmitted signals from the radars are backscattered by magnetic field-aligned irregularities in the ionospheric plasma. The Doppler shift of the signal is then used to calculate the line-of-sight velocity of the plasma. The line-of-sight velocities from all the radars in the network from a given hemisphere are then combined to produce large-scale maps of the convection pattern.

The SuperDARN data is processed in steps and thus there are different levels of data products: First, an autocorrelation function fitting is performed on the raw data for the years 2010-2016 using the FITACF routines, contained in the Radar Software Toolkit. This is the standard procedure for determining line-of-sight velocities from the SuperDARN observations, and we downloaded these data with the FITACF completed. We then spatially and temporally average the line-of-sight data onto an equal-area magnetic latitude and longitude grid in Altitude-Adjusted Corrected Geomagnetic Coordinates (Shepherd, 2014) using an updated version of the gridding technique first introduced by Ruohoniemi and Baker (1998) (SuperDARN Data Analysis Working Group, Thomas, Ponomarenko, Billett, et al., 2018). The recent updates made to the gridding technique in the Radar Software Toolkit versions 4.1 and 4.2 (SuperDARN Data Analysis Working Group, Thomas, Ponomarenko, Billett, et al., 2018; SuperDARN Data Analysis Working Group, Thomas, Ponomarenko, Bland, et al., 2018) include numerous bug fixes as well as implementation of the World Geodetic System 84 reference ellipsoid and the refined Altitude-Adjusted Corrected Geomagnetic Coordinates methodology (Shepherd, 2014). For our analysis we use RST version 4.2. To grid the data we use a two-minute cadence for the records, using the standard empirical height model of Chisham, Yeoman, and Sofko (2008). We limit the slant ranges from 800km to 2000km to exclude ionospheric E-region backscatter and scatter where the error in the location may be very large, as was done by Thomas and Shepherd (2018). When gridding the data, we also exclude data from the secondary channels of the stereo radars (Lester et al., 2004) in order to exclude experimental data. Using RST v4.2 we then utilise the spherical harmonic map fitting method from Ruohoniemi and Baker (1998), to produce an archive of large-scale two-minute northern hemisphere SuperDARN maps using a fitting order of 6. This involves adding model vectors from the climatologies of Thomas and Shepherd (2018), parametrised by the upstream solar wind conditions measured by the ACE satellite (Stone et al., 1998), to stabilise the fit in regions of limited data coverage. The solar wind data is time-lagged to better represent the local conditions using the solar wind propagation time from Khan and Cowley (1999). The Heppner-Maynard boundary (Heppner & Maynard, 1987), which is equivalent to where the zero potential contours are set in the map fitting, is chosen to match the lowest possible latitude for which a minimum of three line-of-sight vectors with velocities greater than 100 ms^{-1} lie along its boundary (Imber, Milan, & Lester, 2013; Thomas & Shepherd, 2018). In our implementation of the fitting routine, we also changed the 50° latitude hard limit on the Heppner-Maynard boundary in RST 4.2 to 40°, to better represent the latitudinal extent of the radar data (see https://github.com/SuperDARN/rst/pull/216

The SuperDARN radar data which we use in this study includes gridded line-of-sight data, as well as the location of the Heppner-Maynard boundary and the cross polar cap potential information. We use data from the years 2010-2016, corresponding to the years of the Thomas and Shepherd (2018) SuperDARN climatological convection model, which means that parameters stemming from the fitted maps, such as the cross polar cap potential and the Heppner-Maynard boundary are estimated to the best of our ability. To analyse the SuperDARN data with respect to the different storm phases, we perform a superposed epoch analysis with the beginning and end of each phase as reference points, and with the duration of each phase normalised by resampling the data to a cadence that yields 100 points in each phase.

3 Results

In this section we show the measurements made during storms with SuperDARN, which we then compare to measurements during times of high solar wind driving when no geomagnetic storm occurs and to measurements made during times when geomagnetic activity is high, irrespective of storm phases.

3.1 Storm phase response

Figure 2 shows how the observations from SuperDARN and the corresponding solar wind data and geomagnetic indices progress through the different storms and storm phases. Each panel shows the initial, main, and recovery phases, on a normalised timescale for a different parameter. Each storm is normalised by the absolute duration of the storm and colourcoded accordingly and the black lines show the median, the lower (25%), and upper (75%) quartiles.

On average, our initial storm phases are much longer (median: 19 hours, 35 minutes) than those from Hutchinson, Wright, and Milan (2011) (6 hours, 59 minutes) (see table S1 in Supporting Information). We find that the main phase (median: 9 hours, 5 minutes; HS2011: 7 hours, 43 minutes) and recovery phase (median: 55 hours, 46 minutes; HS2011: 57 hours, 27 minutes) are comparable in duration, albeit they are very variable from storm to storm. Fig. 2 does not show any clear ordering by storm duration, although some very long storms (in dark red) appear to exhibit the strongest Sym-H minima. There is however no clear trend for the shorter storms.

Fig. 2a shows the Sym-H index for the geomagnetic storm phases. The behaviour of the Sym-H index is defined by our selection criteria and shows that as the convection increases during the main phase of the storm, the ring current enhances, as expected. Fig. 2b shows the average number of gridded SuperDARN velocity vectors, which increases during the main phase, showing that we are likely to get more measurements during this time.

The data for Fig. 2 c, d, and f were extracted from the SuperDARN maps with the spherical harmonic fitting procedure applied to them. The cross polar cap potential, or CPCP, (see Fig. 2 panel d) clearly increases as the main phase of a storm is approached from 40 kV to 80 kV, and is much higher during the main phase (in excess of 100 kV), indicating that plasma convection across the polar cap is higher. During the recovery phase, this then decreases again to $\sim$ 40 kV. Panel c shows that the dawn and dusk cells in the convection maps increase and decrease in a similar way, though the dusk cell is dominant, holding $\sim$2/3 of the potential.

Panel e shows the maximum line-of-sight velocity measured by SuperDARN, which clearly increases during the main phase of a storm. This is further evidence that overall ionospheric convection strength is higher during the main phase of a storm.

Panel f shows the magnetic latitude of the Heppner-Maynard boundary (HMB). The boundary measurement shown in this paper was taken along the nightside meridian. The HMB clearly moves equatorward from the start of the initial phase, until it reaches a minimum latitude near the end of the main phase, which is on average just below 40° of magnetic latitude. It is clear from this panel that a minimum HMB boundary of 40° (instead of the previously used 50°) is required for the main phase of a storm. We estimate the the old limit of 50° would have misplaced the boundary into the 50° bin (instead of equatorward of it) for $\sim$19% of all considered 2-minute intervals for the storms (15.1% (initial phase), 21.0% (main phase), 20.8% (recovery phase)). Although the number of datapoints may seem smaller from Fig. 2 than these percentages, we note that this is due to the normalised timescale. The main phase for example is much shorter than the initial and recovery phases and as such, 21.0% of main phase corresponds to fewer maps than, for example, 21.8% of recovery phase data.

Fig. 2 panel g shows the magnetic latitude coverage of SuperDARN scatter, which also increases during the main phase of the storm. This is to be expected as the convection pattern expands equatorward (see Fig. 2f) and the average number of observations increases during this time (see Fig. 2b).

Panels h to k show solar wind parameters: the total IMF clearly increases during the storm main phases, which is accompanied by a clear increase in the magnitude of the IMF B_Z component (see panel i). Fig. 2 panel j shows the clock angle of the IMF, which is the angle between the IMF B_Y and B_Z component, such that $\pm 180°$ corresponds to purely southward IMF. As this is given by an angle, we have calculated the circular mean instead of the median and upper and lower quartiles, which is shown by the black dots. During the initial phase, the IMF B_Z component is often pointing northward or the B_Y component is dominant over the B_Z component, indicated by a clock angle of $0°$ or $\pm 90°$, respectively. During the main phase, the IMF B_Z component is dominantly negative, as the clock angle is primarily near $\pm 180°$, which corresponds to higher solar wind driving (e.g. Milan et al., 2012).

Fig. 2 panel k shows the solar wind electric field, with respect to Earth, which is a proxy for dayside reconnection and thus solar wind driving of the magnetosphere (e.g. Milan et al., 2012). This clearly increases during the main phase of a storm, as is to be expected by the enhanced convection, shown by panels c, d, and e.

Panel l shows the Auroral Upper and Lower indices (AU and AL, respectively). AL and AU, which are often used as proxies for magnetospheric convection or geomagnetic activity, also show a considerable enhancement during the storm main phase, which gradually declines during the recovery phase. AL in particular is enhanced when convection is the highest. Although, AL and AU are on average less enhanced during the initial phase than during the main phase, the variability is particularly high during the initial phase, and as a result, it can be higher than during the main phase.

Overall, Fig. 2 shows that whilst the observations made with SuperDARN in the initial and recovery phases are very similar, the main phase is characteristically different and convection strength doubles going into the main phase.

3.2 Storm phases, geomagnetically active times, and driven times

Figure 3 shows the probability distribution function for various parameters, which we will now explain in turn. The different functions show the initial phase (orange), the main phase (red) and the recovery phase (green). These are compared to times when the solar wind driving is high, but geomagnetic activity is low (dark blue); and times when geomagnetic activity is high (Sym-H $<$ -80 nT), irrespective of any storm phases (cyan).

Panel a shows the Sym-H component, indicating the ring current strength. We see immediately that geomagnetically active times have the strongest negative Sym-H index measurements associated with them, which was imposed by our criteria. The main phase lies in the middle, covering a similar range of Sym-H as the recovery phase, but spanning lower Sym-H indices. This is again imposed by our criteria of the storm phases. The solar wind driven times (dark blue curve) have on average a weaker negative Sym-H index, as they were selected to be occurring when no geomagnetic storm occurs. The geomagnetically active times (cyan curve) on the other hand drops to zero at a Sym-H of -80nT. The initial phase has the highest Sym-H index, peaking near 0nT, which is again given by the storm phase criteria.

Panel b shows the probability distribution functions for the duration of the storm phases (hence the absence of a dark blue or cyan curve). This panel shows that the main phase is much shorter than the initial and the recovery phase, with the recovery phase lasting on average the longest (as also shown in table S1 in the Supporting Information). We see that the distributions of the duration of the initial and main phases are comparable, whereas the recovery phase duration varies most widely and as such has no clear main peak. It is worth noting that the threshold for determining the end of the recovery phase is important for the duration statistics. We chose this threshold in-line with previous studies, however as can be seen from the example in Fig. 1 a slightly higher threshold would have increased the length of this particular storm.

Panel c shows the average number of gridded vectors per radar per 2 minute SuperDARN convection map. It shows that for driven times when no storm occurs, we are likely to observe less scatter, whereas the PDF for the main phase data shows that we are likely to observe more scatter. Times of high geomagnetic activity (cyan trace) most closely resemble the initial and recovery phase, which are times when the average number of vectors per radar falls below 10. A higher number of vectors corresponds to more ionospheric plasma irregularities being present in the ionosphere. Another possibility is that enhanced electron densities provide enhanced propagation conditions, leading to more direct propagation paths. Either way, this shows that we are likely to get much better coverage of SuperDARN data during the main phase of a storm. This is further discussed in section 4.2.

Panel d shows the probability distribution functions for the maximum line-of-sight velocity observed per 2 minute interval by all SuperDARN radars. It shows clearly that we are most likely to observe high velocities during the main phase. As this parameter represents the upper limit of observed velocities, it indicates that ionospheric convection is highest during the main phase of the storm in comparison to the initial and recovery phases. Highly driven times, where no storm occurs (dark blue) and times of high activity, irrespective of storm phase (cyan) tend to have a lower limit for the observed ionospheric convection speeds. The median observed velocity in panel e shows the same pattern as panel d; the main phase velocities are higher than the velocities for the initial and recovery phase, but what is different in both cases, is that the highly driven times and times of high geomagnetic activity, have a secondary peak. Whilst in panel d this is lower than the main storm peak, in panel e this is higher than the main peaks for the storm phases. This indicates that there is a considerable chance that during driven times and times of high geomagnetic activity, a higher average convection strength is observed than during storms, whilst the maximum observed velocity is more likely to be lower. We suggest that these two distributions are different than the storm distributions as the distributions are chosen independently of the time history of the system. Overall, the median velocity in panel e shows that the upper limit of observed ionospheric convection (panel d) is a good proxy for the overall observed ionospheric convection strength.

Panel f shows the minimum magnetic latitude where scatter observations are made. Each trace shows a triple peak structure, with the main peak in the centre, except the highly driven times and the initial storm phase, which peak at higher latitudes. This means that on average, we are more likely to see radar backscatter during initial phases and driven times confined to higher latitudes, $\sim 60^\circ$, whereas for the other distributions, we can say that the extent of the backscatter has expanded to lower latitudes as ionospheric irregularities are observed there. This is supported by the findings from panel g, which shows the magnetic latitude of the HMB. The probability distribution function is particularly high at lower latitudes during the main phase of a storm and geomagnetically active times in general and extends down to 40° magnetic latitude. This is to be expected, as this coincides with when we are most likely to measure ionospheric backscatter at geomagnetic latitudes of ∼40°.

Panel h shows the CPCP, which is most likely to be highest during the main phase of a storm and during geomagnetically active times, with a peak at approximately 90kV. The recovery phase and initial phase of a storm have the lowest CPCP (with a broader peak at ∼ 40kV), whereas driven times are somewhere in between the two, peaking at ∼70kV. This means that convection is particularly high during the main phase of geomagnetic storms and matches our findings from panels d and e. Panel i shows the minimum and maximum of the electrostatic potential, which indicates if the dusk or dawn cell is dominant. The overall trend from panel h is mirrored here, with the peaks for the main phase and geomagnetically active times lying the furthest apart. What we see here very clearly is a dominance in the minimum of the potential for all traces, meaning that the dusk cell is dominant. This trend is least obvious for the recovery and initial phase, which are thus the most likely to show a balanced convection pattern where the dusk and dawn cells have the same size. We attribute this to the occurrence of sub-auroral polarisation streams (SAPS) (Foster & Vo, 2002) which we discuss further in section 4.3.

Panel j shows the clock angle of the interplanetary magnetic field. The dark blue curve is set to zero between ±90° by our criteria. Both the main phase of the storm and geomagnetically active times maximise for southward IMF, near a clock angle of ±180°. As the red and cyan curves peak at more southward pointing solar wind clock angle than the dark blue curves, it indicates that storms and geomagnetically active times are actually likely to be more extremely driven than the selected driven times. This is because we explicitly exclude storms, and hence the most strongly driven times, from our enhanced driving category, which will thus also include a large proportion of periods where solar wind driving is only moderately enhanced (we only specified that the absolute of the clock angle $> \pm 90°$). In contrast, the initial and recovery phases peak at ±90°, indicating that these periods often have a strong IMF B_Y component attributed to them, with no particular preference between positive or negative.

Panel k shows the electric field of the solar wind with respect to Earth. The peaks of the probability distribution functions for the main phase and the geomagnetically active times are the highest here, which supports the conclusions drawn from panel j that these are times of more extreme solar wind driving. The narrowest peak is the dark blue one, for times of high solar wind driving. Although the peak is slightly lower than the main phase and geomagnetically active time peaks, the broader nature of the latter two imply that enhanced geomagnetic activity occurs for a wide range of solar wind driving conditions. As expected from our inspection of panel j, the initial and recovery phase are more likely to have lower solar wind driving associated with them.

Panel l shows the AU and AL indices, which shows that the geomagnetically active times and storm main phases have a remarkably similar distribution, whereas solar wind driven times without a geomagnetic storm show on average less extreme auroral indices. The initial and recovery phase, are even less likely to see extreme measurements of AL and AU, indicating that the auroral electrojets are weaker during these times.

As already discussed in section 2, we use lower limits for the solar wind conditions (V_{SW}, IMF B_{TOT} and clock angle) to find the periods of high solar wind driving when geomagnetic activity is low. As is shown by Fig. 3 (panels i and j) however, the solar wind driving for these times is not as high as during the main phase of geomagnetic storms. This essentially tells us that when solar wind driving is very high, a geomagnetic storm occurs. From here on, we therefore simply refer to these times as 'driven times'.

3.3 Spatial distribution of ionospheric convection

Figure 4 shows five maps in geomagnetic latitude - magnetic local time (MLT) coordinates that present where the fastest line-of-sight velocities were observed by SuperDARN for the different categories introduced above. Each map is centred on the northern geomagnetic pole with noon to the top of the page. Each grid is normalised by the number of total maps of observations, such that the colours represent the probabilities of observing the fastest flows at each grid point. The grey grid points indicate locations where measurements exist, but no maximum velocities were observed in any of the considered maps. Overall, all maps show some banding, as there are characteristic locations on a geomagnetic map where more scatter is observed due to half-hop and one-and-a-half-hop distances of the radars.

Fig. 4a shows the observations from the initial phase. The data in this map cover the narrowest range of latitudes, with most of the fast flows being observed within 20° to the pole. The fastest flows may occur at almost all local times, with a clearly discernible patch near midnight and sightly more extended patch near noon. Fig. 4b shows the storm main phase, where the majority of fast flows are observed at lower latitudes than in panel (a). Interestingly, the region of fastest flows on the dayside has moved slightly later in MLT, with the fastest flows now rarely occurring on the nightside, although there is some evidence for two bands of fast flow in the pre-midnight sector, at 55°-60° and at around 70°. Fig. 4c shows the recovery phase, which is very similar to the initial phase, although a larger extent of coverage overall (in grey) occurs on the dayside than in Fig. 4a. The dual-bands of pre-midnight fast flows observed during the main phase are also still apparent, although the occurrence of the equatorward band is quite low. Fig. 4d shows the observations for driven times, when no geomagnetic storm occurs. This shows similarities to Fig. 4a and c in terms of fast flow location, i.e. a higher probability of observing the fastest flows on the dayside than the nightside, with the flows generally located closer to the pole than during the main phase of a storm. Lastly, panel (e) shows the observations for intervals of enhanced Sym-H index, irrespective of the storm phase. This shows more similarities to Fig. 4b with a high density of fast flows at lower latitudes. Interestingly, the lower latitude band of pre-midnight fast flows is the dominant region of fast flow in this case, suggestive of a population of flows driven during enhanced geomagnetic activity that are not storm related. We consider the implications of these results further in section 4.3.

Another factor than can affect the nature of the convection patterns is the spatial distribution of the observations that are used to derive them. When very few SuperDARN measurements are present in a map, the map parameters will tend to reflect the climatological map used in the RST map-fitting procedure more closely (in this case the model from Thomas and Shepherd (2018)). As such, it is important to test how robust the distributions such as the ones shown in Fig. 3 in panel f are to changes in the number of observations. Figure 5 shows the magnetic colatitudes of the observed HMB versus different levels of data coverage in the SuperDARN maps (i.e. higher number of gridded radar measurements, n, corresponds to better coverage). Each panel shows a different storm phase and the grey dashed lines indicate the number of maps which exceed the threshold criteria. With this, we can investigate the dependence of the HMB on the number of scatter points per SuperDARN map. The colour coding shows observational density per bin. We see immediately, that the median, shown in Fig. 2, is a good representation, even for maps with low data coverage. All three storm phases show that as the n-threshold increases to higher numbers, the median also increases slightly, but remains approximately within the interquartile range at lower n (e.g. n=100). This means that the Heppner-Maynard boundary is quite well predicted, even at lower n. At very low n (n≤50), there is a lot more variability in the parameter, but the median predicts the HMB well. This means that the estimation of HMB in Thomas and Shepherd (2018) is fairly robust, even for low n for geomagnetic storms. There are some features that do seem to be dependent on the number of measurements. The recovery phase panel in Fig. 5 shows a curious 2 peak structure at n≤350. Comparing the colatitudes at which these peaks are observed with the observations of latitudes in Fig. 2f, we see that this is due to the time-history of the convection pattern during the recovery phase. In the beginning of the recovery phase, the Heppner-Maynard boundary is at low latitudes due to the solar wind driving during the main phase of the storm. As the solar wind driving decreases, the Heppner-Maynard boundary will move to higher latitudes (lower colatitudes), where it then rests and as such we have a secondary distribution in the recovery phase panel in Fig. 5 at lower n. This matches what we see in panels b and e in Fig. 2. Furthermore, the peaks become more defined when the observations per map become greater than 200. This suggests a data coverage threshold may exist at this value. In our subsequent analysis we therefore impose a restriction on the minimum number of data points per map (n≥200). This gives us a good balance between the number of maps included whilst still well constraining the HMB. Furthermore, the same threshold has often been used in the past to filter maps for reliability (e.g. Imber et al., 2013).

Next we inspect flow reversal boundary (FRB), which corresponds to the inner flow boundary where antisunward flows turn to become sunward. At dusk and dawn, this coincides with the location of the maximum and minimum potentials. Whereas the HMB gives us an indication of the size of the whole convection pattern, the locations of the FRB at dusk and dawn gives us an indicator of the size of the polar cap. Figure 6 shows the location of the flow reversal boundary (FRB) against the Heppner-Maynard boundary (HMB) for the three different storm phases. As stated above, for this analysis we only use SuperDARN maps where the number of observations per map, n≥200. We take the colatitude of the FRB as the average of the colatitudes where the minimum and maximum of the electrostatic potential pattern lie, which is equivalent to the boundary between the anti-sunward and sunward flows. Because the asymmetries in the dusk and dawn cell locations are usually within 5° (see Figure S1 in supplementary material), which accounts for most of the spread here, we find that taking the average location between the dusk and dawn cell works well. The dashed line shows the line of unity and the black line shows the line of best fit, obtained by linear regression. We see immediately, that although there is a positive linear correlation between the two flow boundaries, the HMB changes are more extreme than the FRB changes. This means that although the two will change together (i.e. as one increases, the other one increases), the HMB will always change by a larger amount. As Figure 6 shows, this is most pronounced during the recovery phase, where the gradient is flattest. The correlation coefficients are 0.3, 0.5, and 0.2, for the initial, main, and recovery phases, respectively. The best correlation is obtained for the main phase of the storm, where the relationship between the HMB and FRB is the most clear. For information, the linear regression coefficients are provided in table S2 in the Supporting Information. For the recovery phase (see bottom panel in Fig. 6), we see that the majority of the data is clustered around two points with a similar FRB ($\sim$17-10°), but a distinctly different HMB ($\sim$24° and $\sim$37°). We see that these correspond to the two peaks in the recovery phase identified in Fig. 5.

To explore the origin of the two HMB peaks in the recovery phase in Fig. 6, we present in Figure 7 the HMB for the recovery phase of the geomagnetic storms versus the auroral electrojet indices AU, AL and AE. These results clearly show that the HMB peak at 24° colatitude corresponds to times of low electrojet indices ($AU < 150$nT, $AL > -200$nT and $AE < 500$nT), whereas the data from the HMB peak at 37° colatitude in Fig. 6, corresponds to much larger ranges of activity of the auroral electrojet indices. This tells us that when the HMB is at lower latitudes, the auroral electrojet indices are enhanced, which occurs during the expansion and recovery phases of substorms.

Figure 8 shows the relationship of the HMB and FRB throughout the storm phases, but only looking at maps where n$\geq$200. In each case the median is shown in black and the lower (25%) and upper (75%) quartiles in grey. The left panel shows the HMB colatitude in red and the FRB colatitude in blue. The right panel shows the difference between the two throughout the storm phases, colour-coded in the same way as Fig. 2. We see that during the main phase, the convection pattern expands to lower latitudes as both the HMB and FRB colatitudes increase. Not only do they both expand to lower latitudes, but the distance between them also increases. This matches the findings of Fig. 6, which showed that as both the HMB and FRB increase or decrease, the HMB is likely to be changing latitudes at a greater rate. At the beginning of the recovery phase we see both the HMB and FRB decrease abruptly and as a result the distance between them decreases also. We then see the separation between the HMB and FRB decrease further during the recovery phase until similar levels to the initial phase are reached. The FRB however stays fairly constant throughout each phase, except for at the phase changes. This shows that the gradual changes we see throughout each phase in the seperation between the HMB and FRB are due to the HMB moving more rapidly than the FRB. It is worth noting that in comparison with Fig. 2, we have only considered maps where n≥200, which means that the HMB trace has changed slightly. Most notably, the difference between the main phase and the initial phase is larger as the convection patterns, and thus the boundaries, are better defined. During the recovery phase, the interquartile is less well defined, as less data are available. It thus looks as though the interquartile range is more variable, though on average, covers a similar latitude range as previously.

4 Discussion

We have presented ionospheric convection parameters from geomagnetic storm phases, times when solar wind driving is comparable to storms, and high geomagnetic activity, irrespective of storm phase. We show that during the main phase the cross polar cap potential doubles from 40 kV (initial and recovery phases) to 80 kV during the main phase, reaching in some cases in excess of 100 kV. Thus, the main phase shows most enhanced convection. It also shows the highest number of observations per radar, the largest latitudinal extent of the convection, and the fastest flows at lowest latitudes. The geomagnetically active times, irrespective of storm phase, are most similar to the storm main phase, whereas the initial and recovery phase show a weaker response, distinctly different from the main phase. Driven times, when no storm occurs, is somewhere in between two storm populations. We theorise that this is because the strongest driving will always lead to a storm, but that the driving is reduced during the main and recovery phases. We find a positive linear relationship between the HMB and the FRB, although they do not change at the same rate. The HMB changes are larger, especially at the beginning of the main phase, creating an overall larger offset between the HMB and FRB during the main phase than during the other two storm phases. During the recovery phase of a storm, the HMB shows a clear double-peak distribution, which is due to time-variability of the system, such as that associated with substorms. We show that solar wind driving is key to the measured response, but there is a time history effect which gives finer details and differences. We will now discuss these results in greater detail, in particular, how they relate to other relevant studies and prior results.

4.1 Storm duration effects

No obvious relationship between storm strength and the storm phase durations or overall storm duration was observed, except for the duration of the recovery phase and the minimum of the Sym-H at the beginning of the main phase. The Sym-H minimum at the beginning of the main phase is correlated with the amount of driving of the magnetosphere, such as has previously been shown by Gillies et al. (2011). Similarly, the duration of the recovery phase is related to how driven the magnetospheric system is prior to the main phase (e.g. a more intense storm means a longer recovery phase than a less intense storm). As this is not a new result (Gillies et al., 2011), we have not considered this further.

4.2 Number of SuperDARN backscatter echoes

The number of ionospheric scatter echoes increases as we proceed into the main phase of a geomagnetic storm. This is illustrated in Fig. 2, panel b. We reiterate that this actually shows the number of gridded radar velocity vectors, which are derived from averaging multiple Doppler shifted radar echos, but it should scale with the latter such that it can be used as a simple proxy. As the radars are operational all the time and data gaps are rare, we conclude that either the number of scatter points increases because the number of ionospheric magnetic field-aligned irregularities increases or because that enhanced electron densities provide improved propagation conditions, leading to more direct propagation paths and thus enhanced scatter. Although the area observed by the radar ranges stays constant over time, the changes in the latitudinal extent of the convection pattern will change. This may affect the number of backscatter echoes observed, though we do not expect large direct effects of this as radar backscatter is often observed at latitudes below the HMB. The indirect effects, such as the expansion of the convection pattern pulling higher density patches on the dayside to higher latitudes are likely to be larger.

Early SuperDARN results by Milan, Yeoman, Lester, Thomas, and Jones (1997) showed that the number of ionospheric backscatter echoes observed by HF radars changes with location, geomagnetic activity, and season. Milan et al. (1997) found that the frequency and geomagnetic activity dependence of ionospheric backscatter occurrence depends on the range at which it is observed. They compare results from two radars and find that far-range backscatter is likely to decrease in occurrence with an increase in frequency or geomagnetic activity, whereas near range (E-region) scatter is likely to increase. This result was verified by Currie, Waters, Menk, Sciffer, and Bristow (2016) who also showed that it is the main cause of F-region scatter decrease. Here we filter for F-region scatter only by choosing only range gates of 800-2000 km and yet we see the opposite effect. Kane and Makarevich (2010) studied F-region SuperDARN radar echoes with respect to the start of storm sudden commencement, which is the increase seen in the magnetometer measurements or geomagnetic indices prior to a storm and roughly matches our initial phases. They found that ∼12 hours after the start of a storm, the number of observed echoes drops, but find that after storm sudden commencement, the number of radar echoes increases above quiet time numbers. Whilst we do not compare our number of radar echoes to a quiet day curve, we do however also see an increase in the number of radar echoes, but primarily in the main phase. Kumar et al. (2011) studied the spatio-temporal evolution of SuperDARN data during geomagnetic storms using the TIGER Bruny Island radar in the Southern hemisphere. They found that the highest echo occurrence coincides with the start of the storm, which would on average be slightly earlier than our main phase due to their differing criteria. They found that the lowest number of backscatter echoes are measured during the late recovery phase of a storm, which also matches our findings. Kumar et al. (2011) further showed that there is a varying response to F-region echo occurrence measured by the TIGER radar: Short and weak disturbances showed a larger increase in echo numbers at the start of the storm, whereas decreases in occurrences of echoes during the reovery phase were more pronounced for longer storms. Whilst we see the same general trends in the occurrences, we do not see an ordering of echo occurrences with size or duration of the storms. Similarly, Currie et al. (2016) studied the spatial and temporal evolution of backscatter echo occurrence using the TIGER radar in the Southern hemisphere and the Kodiak radar in the Northern hemisphere. They found that during the main phase of a storm, there is a decrease in mid- to far-range scatter, which even though they are similar radar ranges to our observations, we see an increase in the radar echoes. Currie et al. (2016) find that high E-region densities can overrefract rays, which stops them from reaching the F-region and thus decreases the backscatter echo occurrences in the F-region. We infer that our differing results to Kumar et al. (2011) and Currie et al. (2016) are due to the way our observations differ: Whilst Kumar et al. (2011) and Currie et al. (2016) studied occurrences from one and two radars, respectively, we study the observations made by all the SuperDARN radars in one hemisphere. As a result of this, Kumar et al. (2011) and Currie et al. (2016) study the increases or decreases in radar echoes as a function of location, whereas we focus on the global picture here as we are able to observe over all MLTs, as well as latitudes from 90-40°. The increases we see in F-region echo occurrences, in comparison to the decreases seen by Kumar et al. (2011) and Currie et al. (2016) during the storm main phase, indicate that the effects observed by them, namely enhanced E-layers which trap radar signals below the F-region, are not existent at all latitudes and MLTs. We infer that the enhanced E-region layers take some time to propagate and cover larger areas, in particular lower latitudes (see Kumar et al. (2011)), which is why we only see a overall decrease in F-region backscatter occurences during the recovery phase when observing an entire hemisphere.

Wild and Grocott (2008) studied SuperDARN echoes with respect to substorm onsets and found that scatter maximizes just prior to substorm onset. In the nightside ionosphere, backscatter poleward of 70° magnetic latitude is reduced, whereas overall, the radar observations shift to lower latitudes. Thomas, Baker, Ruohoniemi, Coster, and Zhang (2016) used measurements from the global positioning system to show that during a geomagnetic storm, especially during the main phase, the total electron content in the ionosphere increases on average, especially at the start of the main phase. We conclude that in this analysis we are seeing a combination of different effects: As the total electron content in the ionosphere and the size of the convection cells increase, and convection increases, towards and during the main phase of a storm, high density plasma from lower latitudes convects into the polar cap (Thomas et al., 2013). Whilst Thomas et al. (2013) showed that no ionospheric scatter from SuperDARN was observed in the storm enhanced density region extending poleward from mid-latitudes on the dayside, we suspect that plasma patches break off from this due to convection and the net result is a higher number of radar echoes observed on average during the main phase of a storm, which is shown in Fig. 2 (panel b) and Fig. 3 (panel c). The higher ionospheric densities allow better HF propagation conditions in the form of more ionospheric refraction. We also find in Fig. 3 that the amount of scatter during the main phase of a storm is likely to be slightly higher in comparison to driven times. We conclude that this is due to the number of ionospheric irregularities present being related to the level of driving (e.g. Milan et al., 1997), as we have shown that the driving during the main phase of a storm is on average higher than the selected driven times when no storm is observed.

4.3 Occurrence and location of enhanced convective flows

Ionospheric convection is excited by reconnection (Cowley & Lockwood, 1992). When dayside reconnection is dominant, the polar cap expands and when nightside reconnection is dominant, the polar cap contracts. As expected, the ionospheric flows increase accordingly in each case (Walach, Milan, Yeoman, et al., 2017). We would thus expect higher ionospheric convection flows and CPCP for intervals of both higher solar wind driving and enhanced geomagnetic activity. This is shown in Fig. 2, where we see the cross polar cap potential (panel d) and the maximum measured line-of-sight velocities (panel e) increase as solar wind driving (panels k, i, and j) increases. This is also shown in Fig. 3, where we see higher cross polar cap potential (panel h) for times when the solar wind driving is highest (panel j and k). Interestingly, panels (d) and (e) in Fig. 3 do not show this very clearly. If we compare the different storm phases alone, we see that the median measured line-of-sight velocities and the maximum measured line-of-sight velocities are on average highest for the main phase, which matches the aforementioned trends. If we look at the two blue traces in isolation, we see a similar thing: the light blue traces are on average slightly higher than the dark blue ones, which again matches the trends seen in other panels. We do not, however, see this trend when comparing all the traces (i.e. the storm phases in panels (d) and (e) to the blue traces). We suggest a reason for this discrepancy is the time-history of the system. During a geomagnetic storm, the magnetospheric system undergoes a progression through different distinct phases over a prolonged period of time. By definition this includes a pre-conditioning of the magnetospheric and ionospheric system and puts the system into a state where the time-history of the driving and reaction of the system shapes the response. The main difference between the storm-time data and the comparative datasets is this time-history of the system, or in the latter case, the lack thereof. When we collect data for the two blue curves in Fig. 3, no time-history is considered and data is collated where the chosen criteria occur, whereas all the storm data includes by definition a record of the time history of the system. This may explain why the curves in fig. 3 panels (d) and (e) show a different distribution for the storms in comparison to the other two datasets.

The results presented in Fig. 4 demonstrated a number of differences in the location of the fastest flows between our different categories. The initial phase of a storm is associated with intervals of at least modest solar wind driving (see e.g. Figure 3k) which explains the fast flows near noon, which are expected following dayside reconnection. Initial phases are often also associated with solar wind pressure enhancements (e.g. Hutchinson, Wright, & Milan, 2011) which are also known to trigger nightside reconnection (Hubert et al., 2006) and thus drive fast flow on the nightside, as seen here. During the main phase we expect strong solar wind driving, and as such the fastest flows are observed on the dayside. This phase is also associated with an expansion of the convection pattern, as noted in Figure 3g and in agreement with previous studies of polar cap dynamics during storms (e.g. Milan et al., 2009).

The main and recovery phases also displayed some evidence for fast flows at lower-latitudes in the pre-midnight sector. We suggest that these flows are associated with SAPS, which take the form of enhanced westward flows in the midnight-sector thus enhancing the low-latitude region of the dusk convection cell (as noted above in reference to Fig.3). SAPS are known to occur in association with enhanced geomagnetic activity (e.g. Huang & Foster, 2007; Kunduri et al., 2017) and hence an increase in these flows for our storm main phase category is not unexpected. It is worth noting that the SAPS-type flows become the dominant fast flows in the 'enhanced Sym-H' category. SAPS are observed during substorms (e.g. Grocott et al., 2006) as well as geomagnetic storms and hence some of the intervals included in this category may correspond to times of enhanced activity that do not meet the criteria to be classified as a storm. This would also be consistent with the reduced occurrence of fast dayside flows in this category; storm main phases are always expected to be accompanied by enhanced solar wind driving and hence enhanced dayside flows, whereas arbitrary intervals of enhanced geomagnetic activity may not.

It is also worth considering that the difference between the storm main phase and the geomagnetically active categories may be related to the lack of time-dependence in the latter category, as mentioned above. The main and recovery phases are distinctly different, both in terms of the location of enhanced dayside flows, and in the latitude of the pre-midnight fast flow band. Confusing these two phases in any analysis of the ionospheric flows is therefore problematic. In particular, the pre-midnight fast flow bands are both clearly present in the geomagnetically active category, and we suggest that this reflects both the SAPS-type flows associated with the region 2 current system that maps to the inner magnetosphere and the flows driven by reconnection associated with region 1 currents at the open-closed field line boundary. Although clearly linked, there is no requirement for enhancement in these two systems to always be the same (Coxon, Milan, Clausen, Anderson, & Korth, 2014).

4.4 Latitudinal extent of radar observations and the Heppner-Maynard boundary

The minimum latitude at which scatter is observed gives us an idea of how far the convection patterns may expand to, but also what data coverage we can expect for different times. We see from Fig. 2g that the range of latitudes where we observe scatter during the main phase of the storms increases, so we might expect the convection pattern to increase also. This is supported by panel f in Fig. 3, which shows that during the main phase of a storm, we are more likely to see ionospheric scatter at latitudes below 55°. This is particularly important when we compare this to panel g in Fig. 3 or panel f in Fig. 2, which show the magnetic latitude of the Heppner-Maynard boundary. As discussed above, we have added an improvement to the RST code in our analysis that allows the Heppner-Maynard boundary to expand down to 40°, instead of the previously hard-coded limit at 50° that has been used in previous studies. It can be clearly seen that this is crucial for geomagnetic storms, where the convection pattern does often extend below 50° of latitude, especially when the Sym-H index is enhanced, such as during the main phase of a storm. As we only observe moderate geomagnetic storms during this solar cycle, it is possible that this limit could be even lower during extreme geomagnetic storms, though the SuperDARN field-of-views do not extend below 40° of latitude.

We can demonstrate the importance of this issue quantitatively. If we had used a 50° limit for the Heppner-Maynard boundary, the boundary would have been placed too high during ∼17% of all considered 2-minute intervals, which is a considerable proportion of the observation time (for the separate curves this approximately corresponds to: 15% (initial phase), 21% (main phase), 21% (recovery phase), 21% (geomagnetic activity), 7.5% (solar wind driving)). For the geomagnetic storms alone this corresponds to approximately 19% of the time.

In our analysis, the HMB is susceptible to missing data at lower latitudes. This is because there are fewer radars covering the midlatitudes, such that geographical coverage from the midlatitude radars is not as good as from the polar radars (see e.g. Thomas & Shepherd, 2018). The midlatitude radars of course add better coverage, but there are not enough of them to make observations at all longitudes at 40° magnetic latitude. Thomas and Shepherd (2018) noted that the boundary may be misplaced during times when midlatitude radar data is used, and scaled the HMB manually, which is the first large-scale SuperDARN study ever to reflect midlatitude data in the HMB. Having enabled automatic adjustment of the HMB below 50° in our study, we do risk misplacement of the boundary. We therefore explored whether using a radar data coverage threshold would result in a more robust definition of the HMB. We found that a narrowing of the peak in the location of the HMB occurred for n≥200.

4.5 Relationship between the Heppner-Maynard boundary and the flow reversal boundary

We have shown that the FRB and HMB expand equatorward during the main phase of a geomagntic storm, with a subsequent series of smaller expansions and contractions during the recovery phase leading to an overall contraction. Whilst we expect the HMB to lie in the region of the equatorward edge of the auroral oval, the FRB should more closely align with the inner boundary (Walach, Milan, Yeoman, et al., 2017). Milan et al. (2009) presented observations of the auroral oval that revealed the same trend we see in the FRB. The results of Imber et al. (2013) showed that we would expect the HMB also to move with the auroral oval boundary and this is true: we see the same trends with the FRB and HMB, though the HMB moves more rapidly.

Walach, Milan, Yeoman, et al. (2017) showed that the inner auroral oval boundary is a good proxy for the FRB, as the polar cap is expanding and contracting due to solar wind driving and magnetospheric responses. Similarly, the results of Imber et al. (2013) showed that a circle fitted to the brightest parts of the auroral oval, which lies between the FRB and HMB (on average ∼2.8° poleward of the HMB). In their large scale statistical study Imber et al. (2013) considered SuperDARN data only from 2000-2002, before any mid-latitude radars had been deployed in the Northern hemisphere, and showed that even when the auroral oval is expanded to lower latitudes, there is a good correspondence in expansion and contraction between the auroral boundary and the HMB. They note that the small offset between the HMB and the oval latitude ($\sim$2.8°) is greater when the oval is expanded, i.e., during more disturbed magnetic conditions. However, our observations of the FRB and HMB suggest that this offset is actually more extreme, with the FRB-HMB offset increasing to $\sim 20°$ as geomagnetic activity increases.

4.6 Mapping high-latitude ionospheric convection into the magnetosphere

Turner et al. (2019) studied the storm-time morphology of the radiation belts using data from the Van Allen probe mission (Mauk et al., 2013). They showed that during the main phase of a geomagnetic storm and what we have defined as initial phase, tens of keV electrons are enhanced at all considered L-shells (2.5$\leq$L$\leq$6, which corresponds to 39.2° $\leq$geomagnetic colatitude$\leq$24.1° (see Shepherd, 2014)). They find that these enhancements then quickly decay away during the early recovery phase. In most storms ($\geq$90%) higher energy electrons (hundreds of keV) are enhanced at lower L-shells ($\sim$3$\leq$L$\leq\sim$4), which corresponds to geomagnetic colatitudes of 30° to 35.3° in the AACGM coordinate system used here (Shepherd, 2014). These then also decay gradually during the recovery phase. Turner et al. (2019) also showed that relativistic electrons fluxes throughout the outer belt (3.5$\leq$L$\leq$6, corresponding to colatitudes of 32.3° to 24.1°) have a tendency to drop out during the main phase but are then replenished during the recovery phase in an unpredictable way. Their study also shows that electrons with energies >1 MeV are highly likely to show a depletion at all L-shells of the outer belt.

Using equation 1 from Shepherd (2014), we can put these L-shell dependencies into the context of our ionospheric convection observations and the locations of the HMB and FRB. We show that during the main phase of the storm, the HMB sits on average between L-shell 3 (colatitude $\sim$35°) and 2.4 (colatitude 40°) and the FRB sits at L-shell 14.9 (colatitude $\sim$15°) to 10 (colatitude 18°), though this can vary such that the HMB can extend to L-shells of up to 1.7 (colatitudes of up to 50°). This means that during the main phase of the storm, all L-shells considered by Turner et al. (2019), map to regions equatorward of the FRB, but poleward of the HMB in the ionosphere. We thus infer that all the radiation belt regions map to where the ionospheric return flows are occurring, which are the closed field line regions, as expected. Furthermore, we can comment that the outer belt, in particular, matches to regions where we see faster flows in the ionosphere. Comparing Fig. 4 panels (b) and (e) with the results of Turner et al. (2019), we see that the lower latitude band of fast flows attributed to SAPS in our above discussion corresponds to L-shells $\sim$ 3 where the higher energy electrons were measured to enhance and decrease during the storm main and recovery phases. This is consistent with the suggestion made by Califf et al. (2016) that the SAPS electric fields could be responsible for enhancements in 100s keV electron fluxes.

As is shown in Figs. 6 and 8, the offset between the FRB and the HMB varies with geomagnetic activity levels, and even during the different storm phases. Whilst during quieter times, such as the initial phase of a storm, this offset is $\sim$15°, it increases to $\sim$22° during the main phase, when solar wind driving is strongest and then decreases again during the recovery phase. During the main phase, the convection pattern is the most stable, as the difference between the FRB and HMB stays the most constant. This is a significant result, as it has implications for inner magnetospheric dynamics. The HMB is expected to map to the plasmapause, the outer edge of the plasmasphere (e.g. Chen & Wolf, 1972; Maynard & Chen, 1975). This means that as the HMB moves equatorward, the plasmapause is expected to move closer towards the Earth. However, as the ring current increases towards the end of the main phase, the outward pressure in the inner magnetosphere where the ring current lies, increases (Parker, 1957), leading to competing forces. Ultimately, the equatorward expansion of the HMB means that the stagnation point will be inside the plasmasphere, such that a plasmaspheric plume forms (Grebowsky, 1970). An investigation of the low-latitude convection during plume observations is the subject of ongoing work.

4.7 Relationship to substorms and sawtooth events

It was noted above that the time-dependence of the magnetosphere-ionosphere system is likely to be responsible for some of the differences in the convection observed for our storm categories. We see indicators for this in Figs. 5, 6 and 8: During the recovery phase of a storm, the HMB observations fluctuate between two latitudes. A lower latitude right at the start of the recovery phase ($\sim$37° colatitude), which is similar to the location of the HMB during the main phase of the storm, followed by a retreat of the HMB to much higher latitudes and thus a smaller convection pattern ($\sim$24° colatitude). This change appeared to be quite abrupt in Fig. 2, but when only considering maps where n≥200, the change is less abrupt. In this case, we see two clear distributions (e.g. the double peak in Fig. 5). We see in Figs. 2 and 8 that as the solar wind driving decreases and Sym-H becomes less enhanced, the HMB and the FRB move to higher latitudes simlar to at the start of the initial phase. With reference to Fig. 7, we showed that the double-peak distribution in the HMB during the recovery phase is tied to two separate distributions in the auroral electrojet distributions. The high-latitude HMB distribution is limited to low electrojet indices: AU $<$ 150nT, AL $>$ $-$200nT and a low AE $<$ 500nT, which corresponds to low auroral activity. The high HMB distribution on the other hand, corresponds to much higher activity levels. Furthermore, the fast and abrupt changes in the HMB, which we see in the recovery phase in Fig. 8 suggest that the convection pattern is rapidly expanding and contracting, and the majority of the time in the recovery phase is spent in either one of the two states. With the changes occurring very fast in relation to the duration of the recovery phases, we see the resulting double-peak distribution.

We conclude that this result may be related to a phenomenon known as sawtooth events or low-latitude onset substorms (Milan, Walach, Carter, Sangha, & Anderson, 2019; Walach & Milan, 2015). It is common for large, quasi-periodic substorms to occur with a low-latitude onset when the solar wind driving is high and prolonged, and the Sym-H index is enhanced, which are often also termed sawtooth events (Belian, Cayton, & Reeves, 1995; Cai & Clauer, 2013; Milan et al., 2019; Noah & Burke, 2013; Walach & Milan, 2015). Leading up to sawtooth events, solar wind driving and thus the dayside reconnection rate is very high, and as such the polar cap increases in size (Walach & Milan, 2015). Following this, a large dipolarisation, and thus dispersionless injection at geosynchronous orbit is seen, which is followed by a decrease in the polar cap flux (Walach & Milan, 2015). Walach, Milan, Murphy, et al. (2017) showed that as the polar cap decreases in size, after sawtooth event onset, the auroral intensity decreases also, but much more abruptly than for normal substorms. As discussed in section 4.5, we expect the HMB to move in the same way as the polar cap boundary, albeit at lower latitudes. Not only do the changes in the HMB latitude support the finding that these fluctuations are tied to recurring substorms at low latitudes or sawtooth events, but the coinciding auroral electrojet activity also matches that shown by Walach and Milan (2015). Sawtooth events and substorms show an abrupt step-change in the auroral electrojet indices at onset, which for substorms has been shown to be a change of the order of ∼-100nT and for sawtooth events ∼-200nT in AL (Walach & Milan, 2015). We infer from the findings shown in Fig. 7 that these changes in the HMB and coinciding changes in the auroral electroject indices are related to substorm or sawtooth event activity.

5 Summary

We have studied geomagnetic storms from 2010-2016 statistically, in terms of the solar wind driving and ionospheric convection and compared this to geomagnetically active times, as well as times when solar wind driving is high, but geomagnetic activity is very low. This study shows that when studying ionospheric convection during geomagnetically active times, it is crucial to consider data at mid-latitudes. We find that during 19% of storm-time the Heppner-Maynard low-latitude boundary (HMB) of the convection is likely to be below 50°, which previous SuperDARN analyses did not take into account. Specifically, we show for the first time, that it is possible for the HMB to reach latitudes of 40° during the main phase of a storm. We also show that the highest line-of sight velocities measured during the main phase of a storm move to lower latitudes in comparison to the initial phase of a storm. On the dayside, these are most likely to be observed in the post-noon sector, at latitudes around ∼70°. In the dusk to pre-midnight sector, they are most likely to be seen at lower latitudes (≥60°), which is a distinct feature, unique in our dataset to geomagnetically active times (Sym-H≤-80nT) and main phases of storms, and likely related to the subauroral polarisation streams. Generally, the initial phase of a storm shows very similar features to the recovery phase, though the HMB and flow reversal boundary (FRB) are more likely to be observed at lower latitudes during the recovery phase. In fact, the HMB appears to have bimodal distribution during the recovery phase, favouring latitudes of ∼66° and ∼53°, which we attribute to substorm or sawtooth event activity. Not only do the flow boundaries measured by SuperDARN move throughout the storm phases, but the return flow region (the region between the HMB and the FRB) also changes: we see it increase abruptly right before the main phase, then remaining fairly constant and elevated throughout the main phase, before becoming highly fluctuating and then gradually returning to the early initial phase levels. We show that the cross polar cap potential doubles from 40 kV (initial and recovery phases) to 80 kV during the main phase, reaching in some cases in excess of 100 kV. Overall, the SuperDARN observations during times of solar wind driving when geomagnetic activity is low, resemble the initial and recovery phase most closely. On the other hand during geomagnetically active times, irrespective of storm phase, the observations resemble the main phase, but lie somewhere between the data distributions of the main phase, and the initial and recovery phases, as the associated solar wind driving tends to be higher than for the storm initial and recovery phases.

Acknowledgments

All data used for this study is available open-source from non-profit organisations. Solar wind (1-Min averaged OMNI) data is available from https://cdaweb.sci.gsfc.nasa.gov/index.html/ along with all the geomagnetic indices. The authors acknowledge the ude of SuperDARN data. SuperDARN is a collection of radars funded by national scientific funding agencies of Australia, Canada, China, France, Japan, South Africa, United Kingdom and United States of America and we thank the international PI team for providing the data. The authors acknowledge access to the SuperDARN database via the Virginia Tech SuperDARN group and their website (http://vt.superdarn.org/). Other data mirrors are hosted by the British Antarctic Survey and the University of Saskatchewan. The Radar Software Toolkit (RST) to process the SuperDARN data can be downloaded from https://github.com/SuperDARN/rs
M.-T. W. and A. G. were supported by NERC grant NE/P001556/1. M.-T. W. would like to thank Farideh Honary, Mervyn Freeman and Steve Milan for the helpful discussions and useful advice, as well as the members of the SuperDARN DAWG for their tireless effort and support.

References

Baker, D. N., Pulkkinen, T. I., Angelopoulos, V., Baumjohann, W., & McPherron, R. L. (1996). Neutral line model of substorms: Past results and present view. *Journal of Geophysical ...*, *101*(A6), 12975–13010. Retrieved from `http://www.agu.org/pubs/crossref/1996/95JA03753.shtml`

Belian, R. D., Cayton, T. E., & Reeves, G. D. (1995). Quasi-Periodic Global Substorm Generated Flux Variations Observed at Geosynchronous Orbit. *Space Plasmas: Coupling Between Small and Medium Scale Processes, Geophysical Monograph Series*, *86*. doi: 10.1029/GM086p0143

Cai, X., & Clauer, C. R. (2013, oct). Magnetospheric sawtooth events during the solar cycle 23. *Journal of Geophysical Research: Space Physics*, *118*(10), 6378–6388. Retrieved from `http://doi.wiley.com/10.1002/2013JA018819` doi: 10

.1002/2013JA018819
Califf, S., Li, X., Wolf, R. A., Zhao, H., Jaynes, A. N., Wilder, F. D., ... Redmon, R. (2016, June). Large-amplitude electric fields in the inner magnetosphere: Van allen probes observations of subauroral polarization streams. *J. Geophys. Res-Space Phys.*, *121*(6), 5294–5306. doi: 10.1002/2015JA022252
Chen, A. J., & Wolf, R. A. (1972). Effects on the plasmasphere of a time-varying convection electric field. *Planetary and Space Science*, *20*, 483–509. doi: 10.1016/0032-0633(72)90080-3
Chisham, G., Lester, M., Milan, S. E., Freeman, M. P., Bristow, W. a., Grocott, a., ... Walker, a. D. M. (2007). A decade of the Super Dual Auroral Radar Network (SuperDARN): Scientific achievements, new techniques and future directions. *Surveys in Geophysics*, *28*(1), 33–109. doi: 10.1007/s10712-007-9017-8
Chisham, G., Yeoman, T. K., & Sofko, G. J. (2008). Mapping ionospheric backscatter measured by the superdarn hf radars – part 1: A new empirical virtual height model. *Annales Geophysicae*, *26*(4), 823–841. doi: 10.5194/angeo-26-823-2008
Cowley, S. W. H., & Lockwood, M. (1992). Excitation and decay of solar wind-driven flows in the magnetosphere-ionophere system. *Annales geophysicae*, *10*, 103–115. Retrieved from `http://cat.inist.fr/?aModele=afficheN{\&}cpsidt=5295768`
Coxon, J. C., Milan, S. E., Clausen, L. B. N., Anderson, B. J., & Korth, H. (2014). The magnitudes of the regions 1 and 2 birkeland currents observed by ampere and their role in solar wind-magnetosphere-ionosphere coupling. *Journal of Geophysical Research: Space Physics*, *119*(12), 9804-9815. doi: 10.1002/2014JA020138
Currie, J. L., Waters, C. L., Menk, F. W., Sciffer, M. D., & Bristow, W. A. (2016). Superdarn backscatter during intense geomagnetic storms. *Radio Science*, *51*(6), 814-825. Retrieved from `https://agupubs.onlinelibrary.wiley.com/doi/abs/10.1002/2016RS005960` doi: 10.1002/2016RS005960
Foster, J. C., & Vo, H. B. (2002). Average characteristics and activity dependence of the subauroral polarization stream. *Journal of Geophysical Research: Space Physics*, *107*(A12). doi: 10.1029/2002JA009409
Gillies, D. M., McWilliams, K. A., St. Maurice, J.-P., & Milan, S. E. (2011). Global-

scale observations of ionospheric convection during geomagnetic storms. *Journal of Geophysical Research: Space Physics*, *116*(A12). Retrieved from https://agupubs.onlinelibrary.wiley.com/doi/abs/10.1029/2011JA017086 doi: 10.1029/2011JA017086

Gonzalez, W. D., Joselyn, J. A., Kamide, Y., Kroehl, H. W., Rostoker, G., Tsurutani, B. T., & Vasyliunas, V. M. (1994, April). What is a geomagnetic storm? *Journal of Geophysical Research*, *99*, 5771-5792. doi: 10.1029/93JA02867

Gonzalez, W. D., Tsurutani, B. T., & Clúa de Gonzalez, A. L. (1999, Apr 01). Interplanetary origin of geomagnetic storms. *Space Science Reviews*, *88*(3), 529–562. Retrieved from https://doi.org/10.1023/A:1005160129098 doi: 10.1023/A:1005160129098

Grebowsky, J. M. (1970). Model study of plasmapause motion. *Journal of Geophysical Research (1896-1977)*, *75*(22), 4329-4333. Retrieved from https://agupubs.onlinelibrary.wiley.com/doi/abs/10.1029/JA075i022p04329 doi: 10.1029/JA075i022p04329

Greenwald, R. A., Baker, K. B., Dudeney, J. R., Pinnock, M., Jones, T. B., Thomas, E. C., ... Yamagishi, H. (1995). Darn/superdarn. *Space Science Reviews*, *71*(1), 761–796. doi: 10.1007/BF00751350

Grocott, A., Lester, M., Parkinson, M. L., Yeoman, T. K., Dyson, P. L., Devlin, J. C., & Frey, H. U. (2006). Towards a synthesis of substorm electrodynamics: HF radar and auroral observations. *Ann. Geophysicae*, *24*, 3365-3381.

Heppner, J. P., & Maynard, N. C. (1987). Empirical high-latitude electric field models. *Journal of Geophysical Research*, *92*(A5), 4467–4489. doi: 10.1029/JA092iA05p04467

Huang, C.-S., & Foster, J. C. (2007, November). Correlation of the subauroral polarization streams (SAPS) with the Dst index during severe magnetic storms. *J. Geophys. Res.*, *112*(A11). doi: DOI10.1029/2007JA012584

Hubert, B., Palmroth, M., Laitinen, T. V., Janhunen, P., Milan, S. E., Grocott, A., ... Gérard, J.-C. (2006). Compression of the Earth's magnetotail by interplanetary shocks directly drives transient magnetic flux closure. *Geophys. Res. Lett.*, *33*, L10105. doi: 10.1029/2006GL026008

Hutchinson, J. A., Grocott, A., Wright, D. M., Milan, S. E., & Boakes, P. D. (2011, 08). A new way to study geomagnetic storms. *Astronomy & Geo-*

physics, *52*(4), 4.20-4.23. Retrieved from https://dx.doi.org/10.1111/j.1468-4004.2011.52420.x doi: 10.1111/j.1468-4004.2011.52420.x

Hutchinson, J. A., Wright, D. M., & Milan, S. E. (2011). Geomagnetic storms over the last solar cycle: A superposed epoch analysis. *Journal of Geophysical Research: Space Physics*, *116*(9), 1–16. doi: 10.1029/2011JA016463

Imber, S. M., Milan, S. E., & Lester, M. (2013). The heppner-maynard boundary measured by superdarn as a proxy for the latitude of the auroral oval. *Journal of Geophysical Research: Space Physics*, *118*(2), 685-697. doi: 10.1029/2012JA018222

Kamide, Y., Baumjohann, W., Daglis, I. A., Gonzalez, W. D., Grande, M., Joselyn, J. A., ... Vasyliunas, V. M. (1998). Current understanding of magnetic storms: Storm-substorm relationships. *Journal of Geophysical Research: Space Physics*, *103*(A8), 17705-17728. Retrieved from https://agupubs.onlinelibrary.wiley.com/doi/abs/10.1029/98JA01426 doi: 10.1029/98JA01426

Kane, T. A., & Makarevich, R. A. (2010). Hf radar observations of the f region ionospheric plasma response to storm sudden commencements. *Journal of Geophysical Research: Space Physics*, *115*(A7). Retrieved from https://agupubs.onlinelibrary.wiley.com/doi/abs/10.1029/2009JA014974 doi: 10.1029/2009JA014974

Khan, H., & Cowley, S. W. H. (1999, Sep 01). Observations of the response time of high-latitude ionospheric convection to variations in the interplanetary magnetic field using eiscat and imp-8 data. *Annales Geophysicae*, *17*(10), 1306–1335. doi: 10.1007/s00585-999-1306-8

Kilpua, E. K. J., Balogh, A., von Steiger, R., & Liu, Y. D. (2017, Nov 01). Geoeffective properties of solar transients and stream interaction regions. *Space Science Reviews*, *212*(3), 1271–1314. doi: 10.1007/s11214-017-0411-3

Kozyra, J. U., Jordanova, V. K., Borovsky, J. E., Thomsen, M. F., Knipp, D. J., Evans, D. S., ... Cayton, T. E. (1998). Effects of a high-density plasma sheet on ring current development during the november 26, 1993, magnetic storm. *Journal of Geophysical Research: Space Physics*, *103*(A11), 26285-26305. doi: 10.1029/98JA01964

Kumar, V., Makarevich, R., Kane, T., Ye, H., Devlin, J., & Dyson, P. (2011).

On the spatiotemporal evolution of the ionospheric backscatter during magnetically disturbed periods as observed by the tiger bruny island hf radar. *Journal of Atmospheric and Solar-Terrestrial Physics*, *73*(13), 1940 - 1952. Retrieved from http://www.sciencedirect.com/science/article/pii/S1364682611001362 doi: https://doi.org/10.1016/j.jastp.2011.05.001

Kunduri, B. S. R., Baker, J. B. H., Ruohoniemi, J. M., Thomas, E. G., Shepherd, S. G., & Sterne, K. T. (2017, June). Statistical characterization of the large-scale structure of the subauroral polarization stream. *J. Geophys. Res-Space Phys.*, *122*(6), 6035–6048. doi: 10.1002/2017JA024131

Lester, M., Chapman, P. J., Cowley, S. W. H., Crooks, S. J., Davies, J. A., Hamadyk, P., … Barnes, R. J. (2004). Stereo cutlass - a new capability for the superdarn hf radars. *Ann. Geophys.*, *22*(2), 459–473.

Mauk, B. H., Fox, N. J., Kanekal, S. G., Kessel, R. L., Sibeck, D. G., & Ukhorskiy, A. (2013, Nov 01). Science objectives and rationale for the radiation belt storm probes mission. *Space Science Reviews*, *179*(1), 3–27. Retrieved from https://doi.org/10.1007/s11214-012-9908-y doi: 10.1007/s11214-012-9908-y

Maynard, N. C., & Chen, A. J. (1975). Isolated cold plasma regions: Observations and their relation to possible production mechanisms. *Journal of Geophysical Research (1896-1977)*, *80*(7), 1009-1013. Retrieved from https://agupubs.onlinelibrary.wiley.com/doi/abs/10.1029/JA080i007p01009 doi: 10.1029/JA080i007p01009

McPherron, R. L. (1970, oct). Growth phase of magnetospheric substorms. *Journal of Geophysical Research*, *75*(28), 5592–5599. Retrieved from http://doi.wiley.com/10.1029/JA075i028p05592 doi: 10.1029/JA075i028p05592

Mende, S. B., Heetderks, H., Frey, H. U., Stock, J. M., Lampton, M., Geller, S. P., … Lauche, H. (2000). Far Ultraviolet Imaging from the IMAGE Spacecraft. 3. Spectral Imaging of Lyman-α and OI 135.6 nm. In J. L. Burch (Ed.), *The image mission* (pp. 287–318). Springer Netherlands. doi: 10.1007/978-94-011-4233-5_10

Milan, S. E. (2015). Magnetospheric Plasma Physics: The Impact of Jim Dungey's Research. In D. Southwood, S. W. H. Cowley FRS, & S. Mitton (Eds.), *Magnetospheric plasma physics: The impact of jim dungey's research* (pp. 1–271).

doi: 10.1007/978-3-319-18359-6_2

Milan, S. E., Gosling, J. S., & Hubert, B. (2012, mar). Relationship between interplanetary parameters and the magnetopause reconnection rate quantified from observations of the expanding polar cap. *Journal of Geophysical Research*, *117*(A3), A03226. doi: 10.1029/2011JA017082

Milan, S. E., Hutchinson, J., Boakes, P. D., & Hubert, B. (2009). Influences on the radius of the auroral oval. *Annales Geophysicae*, *27*(7), 2913–2924. doi: 10.5194/angeo-27-2913-2009

Milan, S. E., Provan, G., & Hubert, B. (2007, jan). Magnetic flux transport in the Dungey cycle: A survey of dayside and nightside reconnection rates. *Journal of Geophysical Research*, *112*(A1), A01209. doi: 10.1029/2006JA011642

Milan, S. E., Walach, M.-T., Carter, J. A., Sangha, H., & Anderson, B. J. (2019). Substorm onset latitude and the steadiness of magnetospheric convection. *Journal of Geophysical Research: Space Physics*, *0*(0). Retrieved from `https://agupubs.onlinelibrary.wiley.com/doi/abs/10.1029/2018JA025969` doi: 10.1029/2018JA025969

Milan, S. E., Yeoman, T. K., Lester, M., Thomas, E. C., & Jones, T. B. (1997, Jun 01). Initial backscatter occurrence statistics from the cutlass hf radars. *Annales Geophysicae*, *15*(6), 703–718. doi: 10.1007/s00585-997-0703-0

Noah, M. A., & Burke, W. J. (2013, aug). Sawtooth-substorm connections: A closer look. *Journal of Geophysical Research: Space Physics*, *118*(8), 5136–5148. Retrieved from `http://doi.wiley.com/10.1002/jgra.50440` doi: 10.1002/jgra.50440

O'Brien, T., & McPherron, R. L. (2000). Forecasting the ring current index dst in real time. *Journal of Atmospheric and Solar-Terrestrial Physics*, *62*(14), 1295 - 1299. (Space Weather Week) doi: https://doi.org/10.1016/S1364-6826(00)00072-9

Parker, E. N. (1957, Aug). Newtonian development of the dynamical properties of ionized gases of low density. *Phys. Rev.*, *107*, 924–933. Retrieved from `https://link.aps.org/doi/10.1103/PhysRev.107.924` doi: 10.1103/PhysRev.107.924

Ruohoniemi, J. M., & Baker, K. B. (1998). Large-scale imaging of high-latitude convection with Super Dual Auroral Radar Network HF radar observations. *Jour-*

nal of Geophysical Research, *103*(A9), 20797. doi: 10.1029/98JA01288

Selvakumaran, R., Veenadhari, B., Akiyama, S., Pandya, M., Gopalswamy, N., Yashiro, S., ... Xie, H. (2016). On the reduced geoeffectiveness of solar cycle 24: A moderate storm perspective. *Journal of Geophysical Research: Space Physics*, *121*(9), 8188-8202. doi: 10.1002/2016JA022885

Shepherd, S. G. (2014). Altitude-adjusted corrected geomagnetic coordinates: Definition and functional approximations. *Journal of Geophysical Research: Space Physics*, *119*(9), 7501-7521. doi: 10.1002/2014JA020264

Stone, E. C., Frandsen, A. M., Mewaldt, R. A., Christian, E. R., Margolies, D., Ormes, J. F., & Snow, F. (1998, July). The Advanced Composition Explorer. *Space Sci. Rev.*, *86*, 1-22. doi: 10.1023/A:1005082526237

SuperDARN Data Analysis Working Group, P. m., Thomas, E. G., Ponomarenko, P. V., Billett, D. D., Bland, E. C., Burrell, A. G., ... Walach, M.-T. (2018, August). *Superdarn radar software toolkit (rst) 4.2.* Retrieved from `https://doi.org/10.5281/zenodo.1403226` doi: 10.5281/zenodo.1403226

SuperDARN Data Analysis Working Group, P. m., Thomas, E. G., Ponomarenko, P. V., Bland, E. C., Burrell, A. G., Kotyk, K., ... Walach, M.-T. (2018, January). *Superdarn radar software toolkit (rst) 4.1.* Retrieved from `https://doi.org/10.5281/zenodo.1143675` doi: 10.5281/zenodo.1143675

Thomas, E. G., Baker, J. B. H., Ruohoniemi, J. M., Clausen, L. B. N., Coster, A. J., Foster, J. C., & Erickson, P. J. (2013). Direct observations of the role of convection electric field in the formation of a polar tongue of ionization from storm enhanced density. *Journal of Geophysical Research: Space Physics*, *118*(3), 1180-1189. Retrieved from `https://agupubs.onlinelibrary.wiley.com/doi/abs/10.1002/jgra.50116` doi: 10.1002/jgra.50116

Thomas, E. G., Baker, J. B. H., Ruohoniemi, J. M., Coster, A. J., & Zhang, S.-R. (2016). The geomagnetic storm time response of gps total electron content in the north american sector. *Journal of Geophysical Research: Space Physics*, *121*(2), 1744-1759. doi: 10.1002/2015JA022182

Thomas, E. G., & Shepherd, S. G. (2018, apr). Statistical Patterns of Ionospheric Convection Derived From Mid-latitude, High-Latitude, and Polar SuperDARN HF Radar Observations. *Journal of Geophysical Research: Space Physics*, *123*(4), 3196–3216. Retrieved from `http://doi.wiley.com/10.1002/`

2018JA025280 doi: 10.1002/2018JA025280

Turner, D. L., Kilpua, E. K. J., Hietala, H., Claudepierre, S. G., O'Brien, T. P., Fennell, J. F., ... Reeves, G. D. (2019). The response of earth's electron radiation belts to geomagnetic storms: Statistics from the van allen probes era including effects from different storm drivers. *Journal of Geophysical Research: Space Physics*, *0*(0). doi: 10.1029/2018JA026066

Walach, M.-T., & Milan, S. E. (2015). Are steady magnetospheric convection events prolonged substorms? *J. Geophys. Res.*, *120*(3), 1751–1758. doi: 10.1002/2014JA020631

Walach, M.-T., Milan, S. E., Murphy, K. R., Carter, J. A., Hubert, B. A., & Grocott, A. (2017). Comparative study of large-scale auroral signatures of substorms, steady magnetospheric convection events, and sawtooth events. *Journal of Geophysical Research: Space Physics*, *122*(6), 6357-6373. Retrieved from https://agupubs.onlinelibrary.wiley.com/doi/abs/10.1002/2017JA023991 doi: 10.1002/2017JA023991

Walach, M.-T., Milan, S. E., Yeoman, T. K., Hubert, B. A., & Hairston, M. R. (2017). Testing nowcasts of the ionospheric convection from the expanding and contracting polar cap model. *Space Weather*, *15*(4), 623-636. doi: 10.1002/2017SW001615

Wanliss, J. A., & Showalter, K. M. (2006). High-resolution global storm index: Dst versus SYM-H. *Journal of Geophysical Research*, *111*(A2), A02202. Retrieved from http://doi.wiley.com/10.1029/2005JA011034 doi: 10.1029/2005JA011034

Wild, J. A., & Grocott, A. (2008). The influence of magnetospheric substorms on superdarn radar backscatter. *Journal of Geophysical Research: Space Physics*, *113*(A4). Retrieved from https://agupubs.onlinelibrary.wiley.com/doi/abs/10.1029/2007JA012910 doi: 10.1029/2007JA012910

Yokoyama, N., & Kamide, Y. (1997). Statistical nature of geomagnetic storms. *Journal of Geophysical Research: Space Physics*, *102*(A7), 14215-14222. doi: 10.1029/97JA00903

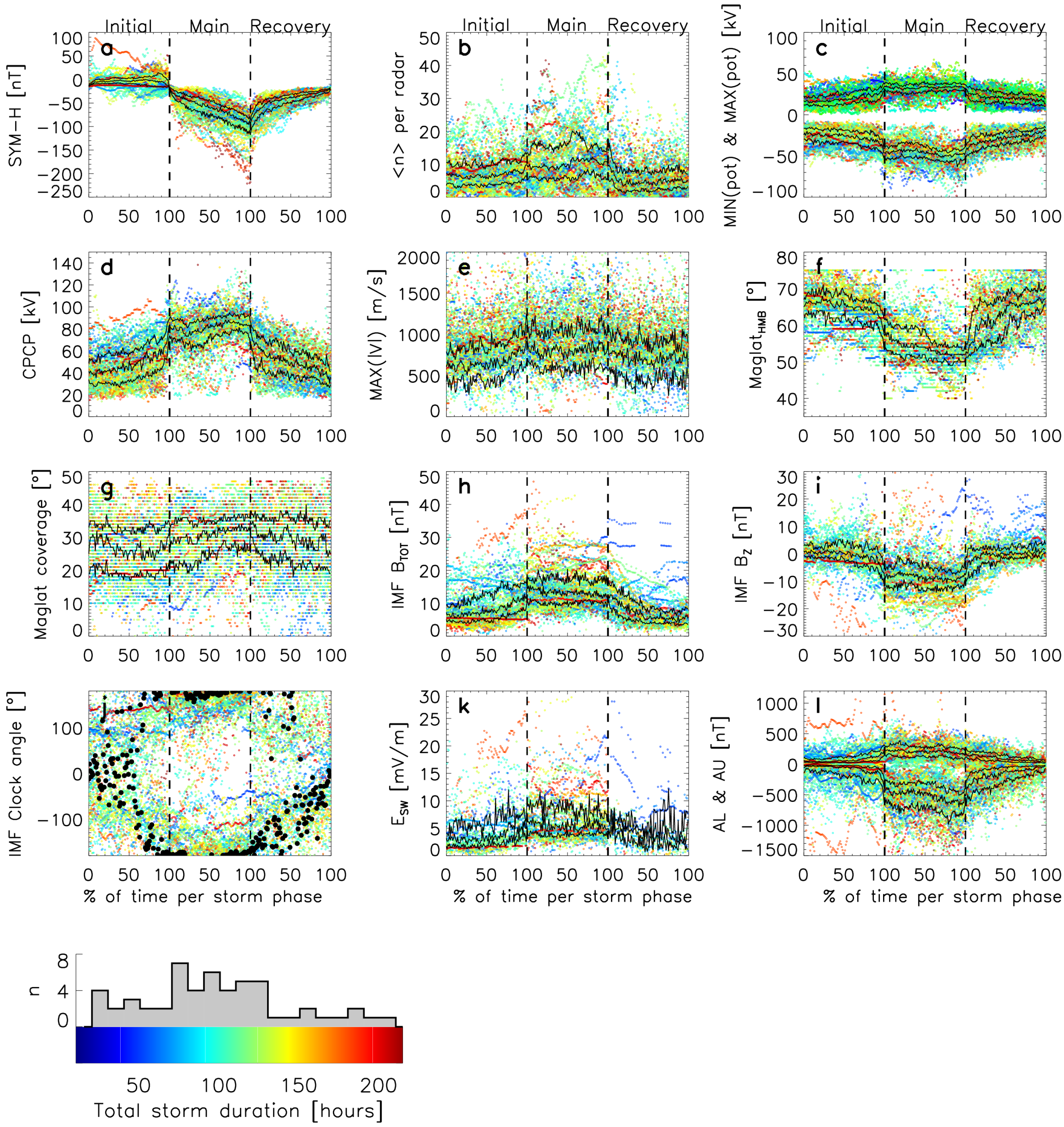

Figure 2. Different parameters, showing the progression through the storm phase. Each panel shows the initial, main, and recovery phases of the storm on a normalised time scale with individual storms colourcoded by their absolute duration, which is indicated by the colour scale. The black lines show the lower and upper quartiles (25% and 75%), and the median. Panels a to l show, respecitvely: SYM-H index, average number of scatter points per radar; minimum and maximum potential from the SuperDARN maps; cross polar cap potential from the SuperDARN maps; maximum radar line-of-sight speed; magnetic latitude of the Heppner-Maynard boundary; magnetic latitude extent of coverage; total magnetic field in the IMF; magnetic field component of the IMF in the Z-direction; IMF clock angle; electric field of the solar wind; AL & AU indices.

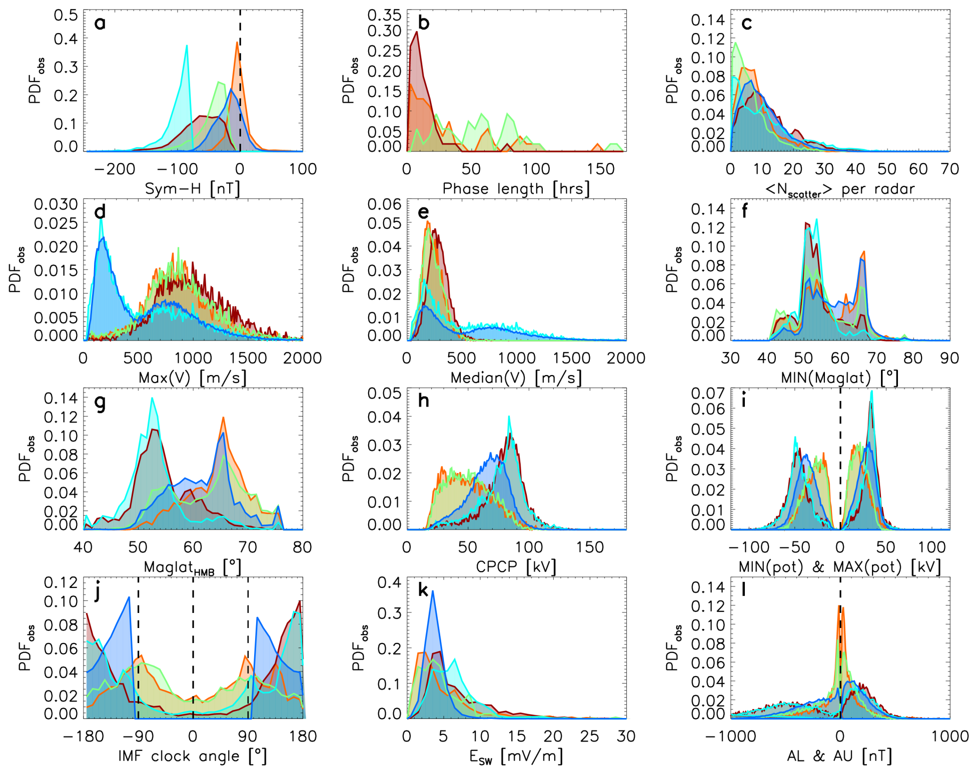

Figure 3. Different parameters, showing the Probability distribution functions for the storm phases (orange: initial phase, red: main phase, green: recovery) in comparison with driven times, but where no storm occurs (dark blue), and geomagnetically active times, irrespective of storm phase (cyan). Panels a to l show: Sym-H index; Phase duration; average number of scatter points per radar; the maximum velocity measured by the radars; the median velocities; the minimum magnetic latitude where SuperDARN scatter is observed; the magnetic latitude of the Heppner-Maynard boundary; the cross polar cap potential; the maximum and minimum potential of the convection cells; the IMF clock angle; the electric field in the solar wind, with respect to the Earth; AL and AU.

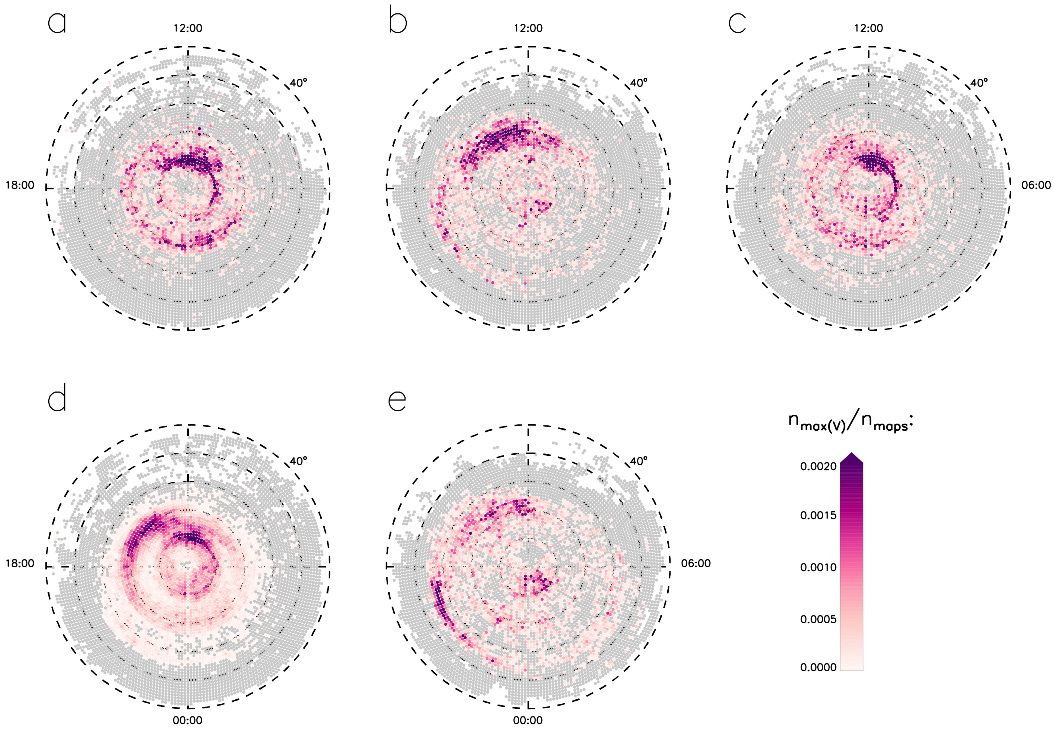

Figure 4. Polar maps in magnetic latitude - magnetic local time coordinates showing the locations of where the fastest flows are observed for each activity type (a: initial phase, b: main phase, c: recovery phase, d: driven times, e: enhanced Sym-H index, irrespective of storm phase). Noon is to the top, and dusk to the left. Grey gridpoints indicate locations where data was available, but none of the maximum velocities were measured.

.

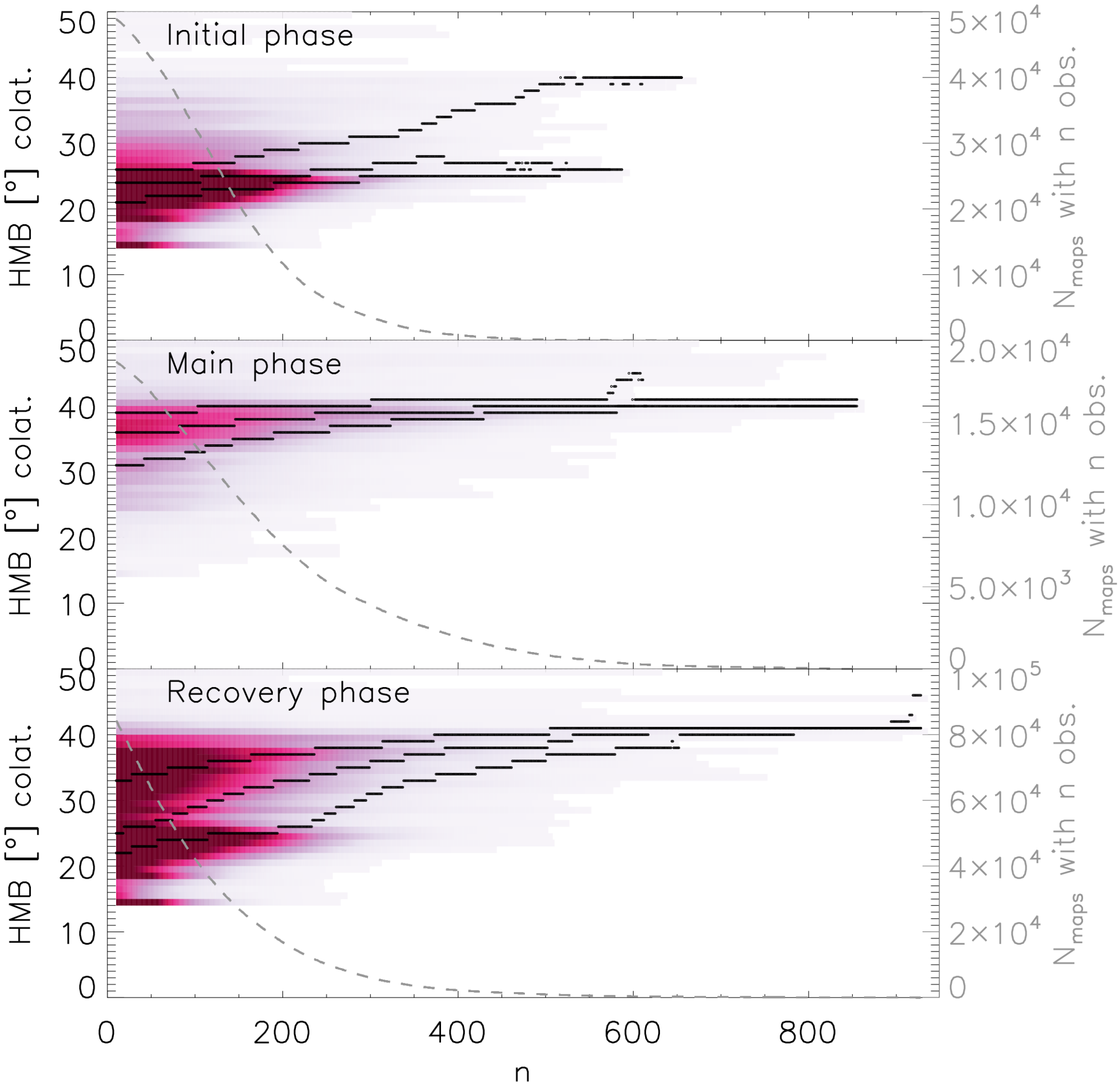

Figure 5. Heppner-Maynard boundary (HMB) of the maps versus the number of obervations per map (n). The median and the lower and upper quartiles are shown by the black dots and the colour saturation indicates observational density. The grey dashed curve indicates the number of maps per n per storm phase. The bin between $0 < n < 10$ was left intentionally blank and would correspond to the distribution shown in Fig. 3f.

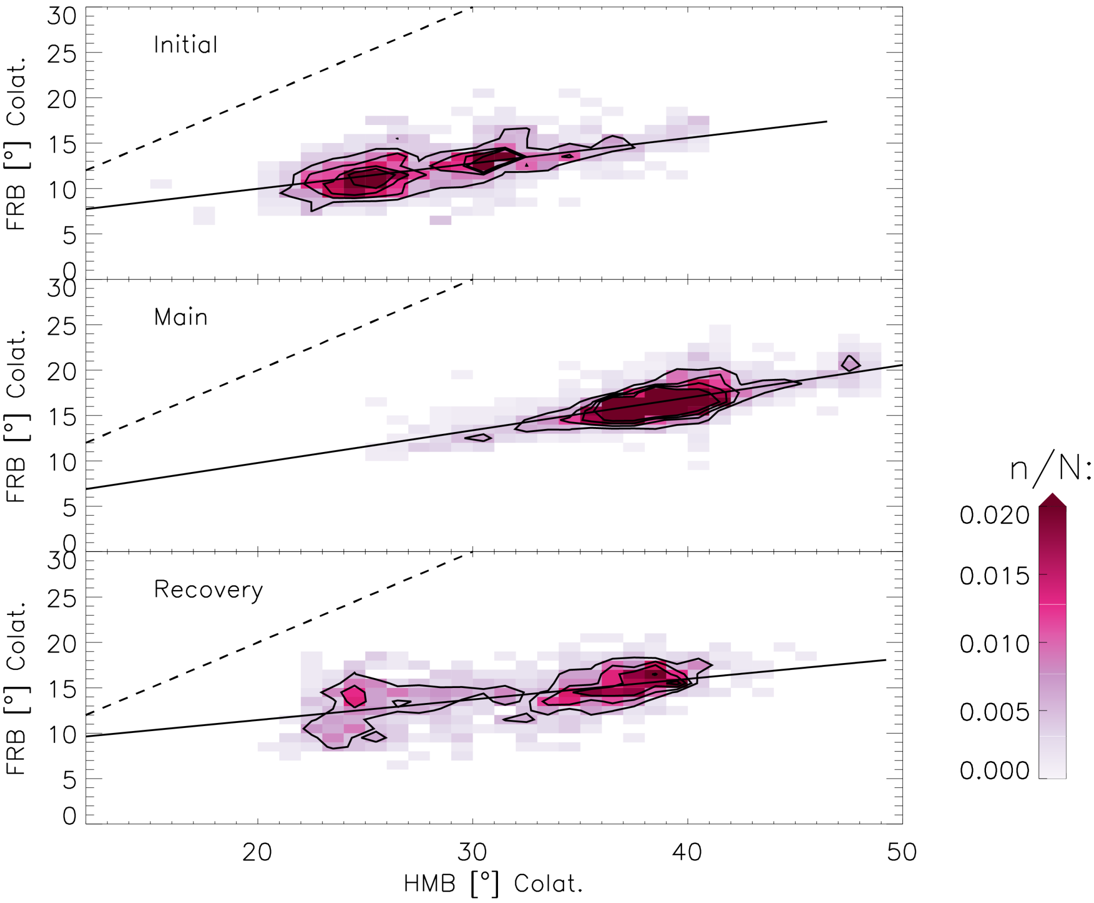

Figure 6. Colatitude location of the flow reversal boundary (FRB) against the Heppner-Maynard boundary (HMB) during the three phases of geomagnetic storms (only using maps where n≥200). The dashed black lines show the line of unity and the black contours correspond to where the normalised datapoint density corresponds to 0.005, 0.01, 0.015 and 0.02.

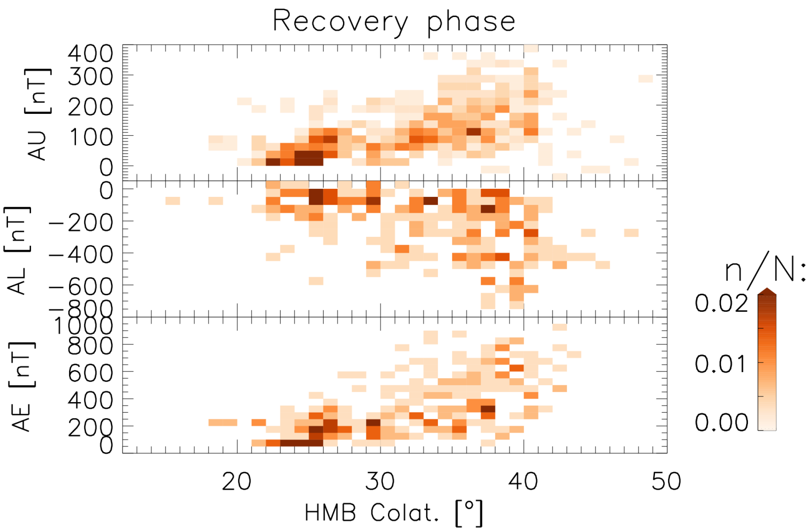

Figure 7. Colatitude location of the Heppner-Maynard boundary (HMB) during the recovery phase versus AU, AL and AE (only using maps where n≥200).

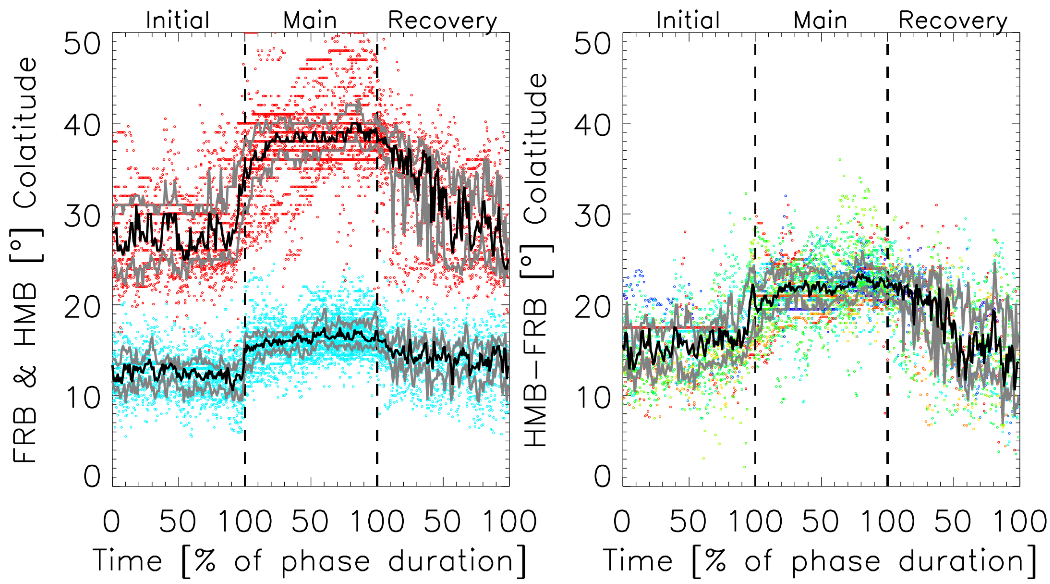

Figure 8. Heppner-Maynard boundary (red) and flow reversal boundary throughout the different storm phases (blue) on the left and the difference between the two (right), colourcoded in the same way as Figure 2, but only using maps where n≥200. The solid lines show the median (black) and 25% and 75% quartiles (grey).